EUROPEAN ORGANIZATION FOR NUCLEAR RESEARCH

CERN-SL-2000-010 AP

LONGITUDINAL IMPEDANCE FROM FERRITE

L.Vos

Abstract

General expressions for the complex permeability of ferrites are derived. The imaginary part of this permeability, related to magnetic losses, is of particular interest. It leads to a resistive impedance that extends in frequency as high as ~ 10 *GHz*. This impedance initially rises with frequency from zero to a maximum and then decreases again due to the decreasing penetration depth. The longitudinal resistive impedance is computed for the ferrites installed in the SPS machine. It amounts to $Z/n < 1\ \Omega$ at 1.5 *GHz*, which is negligible as compared to the measured values of Z/n which range from 20 to more than 30 Ω. The contribution of the ferrites to the imaginary part of longitudinal impedance is computed as well. It is capacitive at 1.5 *GHz* and its magnitude is of the same order as the resistive part.

Geneva, Switzerland
March , 2000

1 Introduction

The magnetic properties of ferrites have been thoroughly studied in the past [1] and the theory is well established in the face of experimental evidence. In section 2, the relevant formulae are presented to find the expressions for the contribution of unshielded ferrite items to the longitudinal impedance. The theory that allows the derivation of these formulae can be found in references [1-6]. The same terms and notations were used as in these references. The contribution of the ferrite that is typical for kicker magnets extends to frequencies in the 10 *GHz* region. This was the main motivation to find the expression for the longitudinal resistive impedance arising from the ferrite in the kicker magnets of the SPS machine and to compare it with the values that have been measured in the past for the high frequency (around 1.5 *GHz*) resistive part of the broad-band impedance.

2 Magnetic properties of ferrites

The basic property of ferrite is the fact that magnetic fields are present in the material at all times. In the absence of external fields no field escapes from a sample. This is due to the fact that the internal fields arrange themselves in so-called Weiss domains such that the field lines form closed loops. Each domain is characterised by a direction of its internal magnetic field. The organisation of the domains in the sample obeys the classical rule of minimal total energy. A magnetic field applied from the outside will tend to turn the internal magnetic field vectors towards the external field direction. The resulting magnetic induction in the sample in the direction of the external excitation can be much larger than the induction obtained in free space by the same excitation. That is the origin of the high permeability of these materials.

Consider an electron with spin that circulates on an atomic orbit in a magnetic field B. The moving electron generates circular currents that cause magnetic moments μ_M . The interaction between the magnetic moment of the electron with the field B will lead to a precession with a frequency given by [1]:

$$\omega = \frac{\mu_M}{J} B = \gamma B, \tag{1}$$

where J is the angular momentum of the electron. The magnetic moment is :

$$\mu_M = g \frac{e}{2m_e} J, \tag{2}$$

where m_e is the mass of the electron and g is the gyro-magnetic factor. For the orbital magnetic moment g=1 and for the spin g~2. In ferrites the spin magnetic moment largely dominates [2,3] such that :

$$\omega = \frac{e}{m_e} B. \tag{3}$$

The organisation of the electron spins in ferrites gives rise to an internal field in the domains which is called anisotropy field B^A [2,3]. The anisotropy is a direct consequence of the crystallographic structure of ferrites. The relation between this field and the field level at which the ferrite saturates B_s is [3] :

$$B^A = \frac{2}{3}\frac{B_s}{\mu_i - 1}, \tag{4}$$

where μ_i is the low frequency or initial relative permeability of the ferrite.

The internal field B^A defines a precession frequency (ferri-magnetic resonant frequency) for the magnetic moments of the spinning electrons of [3]:

$$\omega_r = \gamma B^A = \gamma \frac{2}{3}\frac{B_s}{\mu_i - 1}. \tag{5}$$

The ferri-magnetic resonator is damped. The damping is related to movements of the domain walls to which an equivalent mass [4,5] can be attributed. Hence it will absorb energy from an external excitation source. The energy dissipation will be at its peak when the frequency of the excitor is equal to the resonant frequency. The bandwidth of the resonator is a measure for its damping. Experimentally it has been shown that the time constant of the process (which is the inverse of its bandwidth) is [3,5]:

$$\tau = \frac{\mu_i - 1}{\gamma B_s} = \frac{2}{3\omega_r} \quad ; \quad \Delta\omega = \frac{3}{2}\omega_r \tag{6}$$

No dissipation will occur when the frequency of the excitation is higher than [3]:

$$\hat{\omega} = \gamma B_s = \frac{e}{m_e} B_s. \tag{7}$$

The relative permeability $\bar{\mu}$ can in general be written as a complex quantity which depends on frequency :

$$\bar{\mu} = \mu' - j\mu''. \tag{8}$$

The imaginary part μ" is related to the dissipative part of the process just described and can be derived from Eq. 6. The real and imaginary part of the complex permeability are linked by the Kramers-Kronig relations [3]. It implies that if one of the two components is known by computation or measurement, then the other one can be evaluated. It turns out that the complex relative permeability in excess of the permeability of free space is given by the following simple expression :

$$\boxed{\frac{\bar{\mu}}{\mu_i - 1} = \frac{1}{1 + j\omega\tau}} \tag{9}$$

with $\tau = \frac{m_e}{e}\frac{\mu_i - 1}{B_s} = \frac{\mu_i - 1}{\hat{\omega}}$. This formula is valid for $0 \le \omega \le \hat{\omega} = \frac{e}{m_e} B_s$. The polar plot of the relative permeability normalised to μ_i in the complex plane is half a unit circle familiar in the literature about ferri-magnetism [5,6].

3 Examples and applications

Let us first look at the magnetic properties of some ferrites that are typical for kicker magnets. They are of the low conductivity *NiZn* ferrite family. The saturation field is B_s = 0.35 *T* which defines the maximum frequency where ferri-magnetic losses can occur (Eq. 7) :

$$\frac{\hat{\omega}}{2\pi} = 9.8\ GHz\,.$$

The grades of these ferrites differ in their initial permeability μ_i. As an example consider two different grades manufactured by Philips : *4A4* and *4A11*. The measured magnetic properties are shown in Fig. 1 [7].

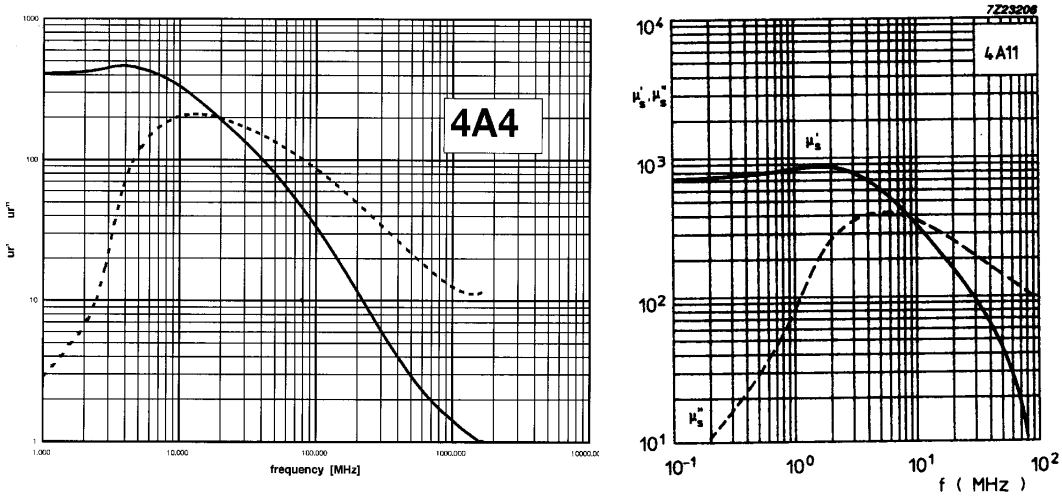

Figure 1 : Real (full) and imaginary (dashed) relative permeability for the series equivalent circuit of typical ferrites

From these plots the ferri-magnetic resonant frequency can be estimated. The initial permeability is taken as the maximum of the real relative permeability. The time constant τ is derived from the frequency where the real and imaginary parts are equal. Notice that the maximum of μ", i.e. maximum of dissipation, occurs at a lower frequency, in accordance with Eq. 6. In Table 1 the results obtained in this way are compared with the theoretical resonant frequencies computed with Eq. 5.

Table 1: Initial permeability and resonant frequency obtained from Fig. 1 and theoretical resonant frequencies from Eq. 5.

	Material	*4A4*	*4A11*
	μ_i - 1	460	850
	$1/2\pi\tau$ *(MHz)*	20	9
	$\omega_r/2\pi$ *(MHz)*	13.3	6
Eq.5	$\omega_r/2\pi$ *(MHz)*	14.2	7.7

It is interesting to compare the measured and the computed imaginary part of the permeability for material *4A4* for which data are available well beyond 1 *GHz*. That comparison is shown in Fig. 2.

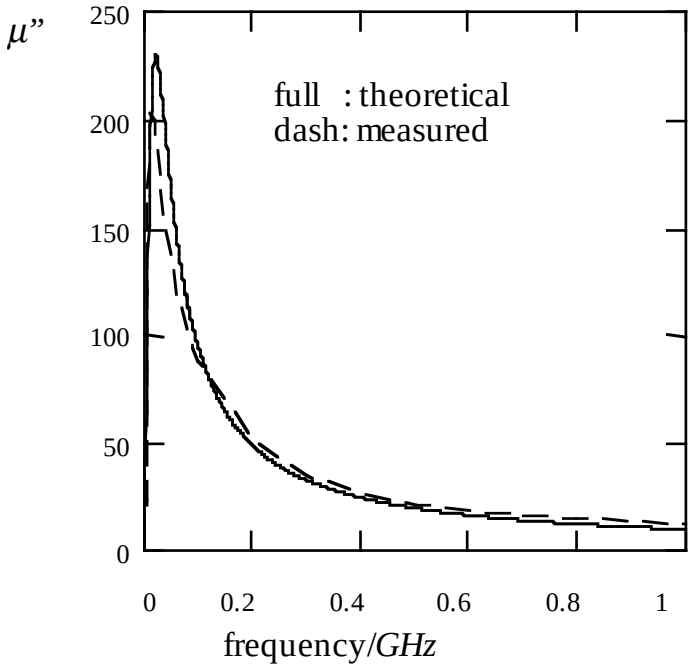

Figure 2 : Measured (Fig. 1) and computed (Eq. 9) imaginary relative permeability for *4A4* ferrite.

The fit is remarkably good for frequencies larger then 100 *MHz*, which is the relevant part for the SPS as will be seen later. The formula for the complex permeability can be simplified for that frequency range since $\omega\tau >> 1$:

$$\frac{\bar{\mu}}{\mu_i - 1} = \frac{1}{1 + j\omega\tau} \approx \frac{1}{j\omega\tau}, \tag{10}$$

and

$$\bar{\mu} = \frac{\hat{\omega}}{j\omega} \quad \Rightarrow \quad \mu'' = \frac{\hat{\omega}}{\omega} = \frac{eB_s}{m_e\omega}. \tag{11}$$

Note that, in this approximation, the real part of the permeability μ' vanishes and the imaginary part is independent of the initial permeability; it only depends on frequency and on a single material constant, i.e. B_s.

4 Impedance of ferrite

The surface impedance of ferrite with infinite thickness is (see also [11]):

$$Z_{surface} = \sqrt{\frac{j\omega\mu}{j\omega\varepsilon + \sigma}}. \tag{12}$$

The complex permeability of ferrite $\mu = \mu_0(\mu' - j\mu'')$ where $\mu_0 = 4\pi * 10^{-7}$ *Vs/Am* is the permeability of free space, can be computed from Eq. 9. The complex permittivity of ferrite is $\varepsilon = \varepsilon_0(\varepsilon' - j\varepsilon'')$ where $\varepsilon_0 = 8.8 * 10^{-12}$ *As/Vm* is the permittivity of free space. The real part of the relative permittivity is fairly constant with frequency and amounts to $\varepsilon' = 12$, a typical value for ceramic-like materials [3,8]. The imaginary part of the relative permittivity of ferrite is very small and can be neglected. The conductivity of ferrite is $\sigma = 1/\rho$, where ρ is the resistivity. The issue is to decide which value to assign

to the resistivity. Ferrite consists of large domains of fairly well conducting material which are separated by thin layers of relatively poor conducting substance [3,7]. The resistivity of ferrite tends towards the resistivity of the large domains for very high frequency [7]. In the present approach, it is assumed that the conduction losses are dominated by the losses in the domains and consequently, the conduction losses in the thin layers hardly contribute. It was therefore decided to use the high frequency intrinsic resistivity in the following. It depends critically on the chemical composition and its limit is not so well defined. In [3] a lower value of $\rho = 10\ \Omega m$ is mentioned while the manufacturer quotes an approximate value of $\rho = 30\ \Omega m$[7]. The last value has been used in the numerical calculations. The real and imaginary parts of the surface impedance are shown in Fig. 3. The contribution of a non-zero conductivity to the resistive part of the impedance is indicated as well.

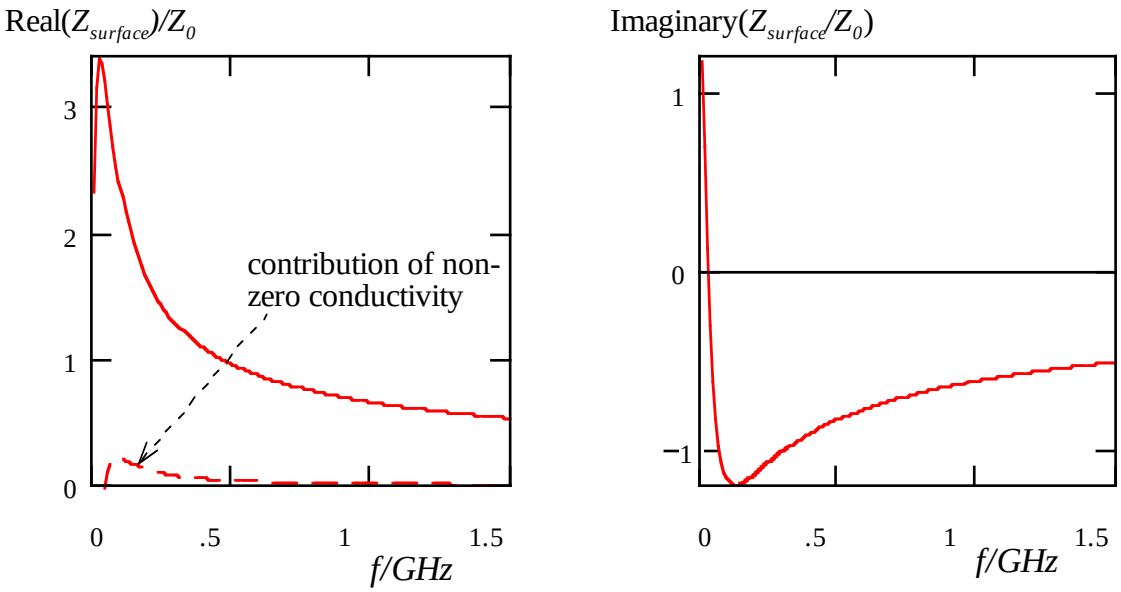

Figure 3 : Surface impedance $Z_{surface}$ (real part on the left, imaginary part on the right) of ferrite between 10 *MHz* and 1.5 *GHz* normalised with $Z_0 = 120\pi\ \Omega$, the impedance of free space.

It may be interesting to note that the impedance is capacitive for frequencies higher than 35 *MHz*. This was first pointed out to the author by H. Tsutsui.

The transverse propagation constant γ in ferrite of the electro-magnetic waves generated by an ultra-relativistic beam ($\beta = 1$) is :

$$\gamma = \alpha + j\beta = \sqrt{j\omega\mu(\sigma + j\omega\varepsilon) - (\omega/c)^2}\ , \qquad (13)$$

where α is the attenuation constant and β the phase constant in classical notation of transmission line theory. The skindepth is the inverse of α and is shown in Fig. 4. The dependence of $1/\alpha$ on the initial relative permeability μ_i turns out to be very small and will be neglected. The wavelength $\lambda = 2\pi/\beta$ is shown as well.

The surface resistance of ferrite in a kicker magnet can be computed with Eq. 12 since the skindepth is much smaller than the actual thickness of the ferrite (at least 40 *mm*), The impedance per unit length of a ferrite torus with inner radius *b* is then :

$$z = \frac{1}{2\pi b}\sqrt{\frac{j\omega\mu}{j\omega\varepsilon+\sigma}}. \tag{14}$$

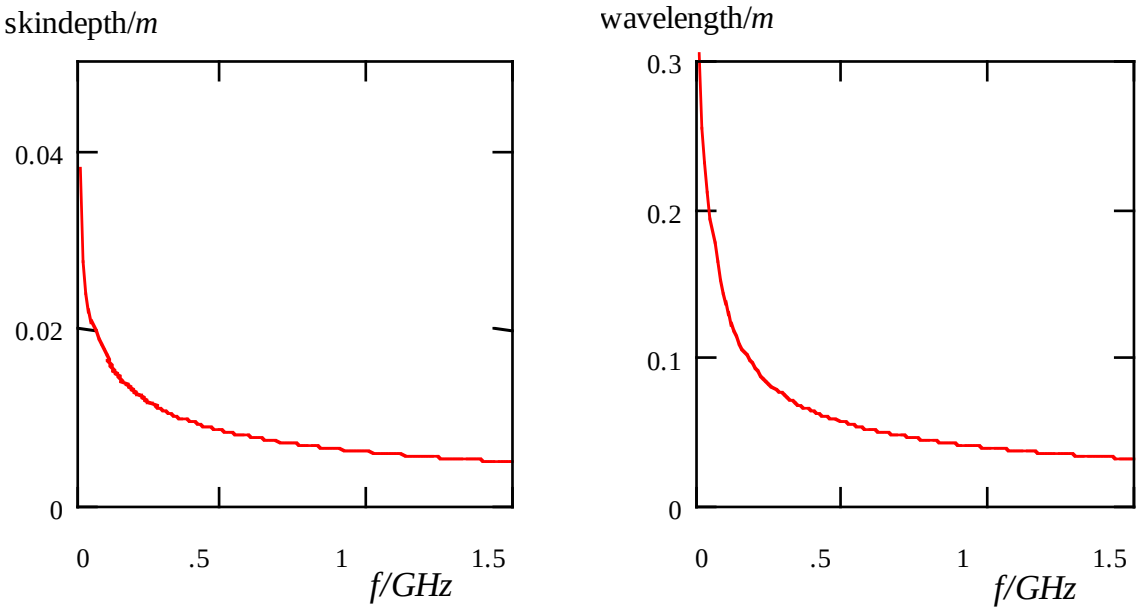

Figure 4 : Skindepth and wavelength in ferrite from 10 *MHz* to 1.5 *GHz*.

The ferrite in kickers is arranged in a parallel plate geometry while Eq. 14 is valid for a cylindrical geometry. The parallel plate arrangement is replaced by an equivalent cylinder for computational ease. The radius of the cylinder is such that the integrals of the unperturbed fields on the inner face of the cylinder and on the parallel plate geometry are the same. The equivalent radius is then :

$$b_{eq} = \frac{\pi}{2}b, \tag{15}$$

where b is the inscribed radius of the parallel plate geometry. The ferrite is not exposed to the beam over 2π but only over a fraction ν of this angle and the impedance is reduced accordingly. This then yields for the impedance per unit length of ferrite :

$$z = \frac{\nu}{\pi^2 b}\sqrt{\frac{j\omega\mu}{j\omega\varepsilon+\sigma}}. \tag{16}$$

It is clear that the model is simplified, but it was selected for its analytical simplicity and its ease in numerical computations.

5 Longitudinal impedance from ferrite in the SPS

The interaction of the beam with the resistive part of the ferrite impedance leads to power dissipation and heating. The results of two thermal experiments on a MKE kicker magnet are analysed in Appendix A.

In order to estimate the contribution of the ferrite to the longitudinal impedance of the SPS it is useful to express Eq. 16 in terms of *Z/n* and make the sum over all kicker magnets installed in the machine:

$$Z/n = \frac{c}{\pi^2 \omega R} \sqrt{\frac{j\omega\mu}{j\omega\varepsilon + \sigma}} \sum \frac{l_i \nu_i}{b_i}, \qquad (17)$$

where R =1100 *m* is the radius of the SPS machine, l_i is the length of the *i*-th magnet with coverage factor ν_i and inscribed radius b_i. Table 2 shows the inventory of the ferrite fast kickers of the SPS at the time when the machine was operated as a proton-antiproton collider. In fact, this corresponds to the layout of the machine, when measurements on the high frequency turbulence were performed [9,10].

Table 2: Geometrical constants of ferrite fast kicker magnets of the SPS

magnet name	number	l_i	aperture H*V	b_i	ν_i	ν_i/b_i
		m	*mm*mm*	*mm*		m^{-1}
MKP	2	2.836	100*61	30.5	0.65	21
MKP	1	2.836	140*54	27	0.77	29
MKA	3	0.709	140*54	27	0.77	29
MKDV	1	2.560	75*56	37.5	0.41	11
MKDV	1	2.560	83*56	41.5	0.38	9
MKDH	3	1.256	97*56	28	0.67	24
MKE	7	1.658	135*32	16	0.85	53
MKQH	1	0.483	135*33.9	17	0.85	50
MKQV	1	1.027	102*56	51	0.32	6

The values in the last column (ν_i/b_i) can be considered as an impedance per unit length in arbitrary units. Using these numbers in Eq. 17 yields :

$$Z/n = \frac{c}{\pi^2 \omega R} \sqrt{\frac{j\omega\mu}{j\omega\varepsilon + \sigma}} 1050 \qquad (18)$$

The plot of the longitudinal impedance *Z/n* from the ferrite kickers in the SPS is shown in Fig. 5. The computation is stopped near the cut-off frequency of the SPS vacuum chamber, that is ~ 1.5 *GHz*. Higher frequencies propagate in the vacuum chamber and loose synchronism with the beam.

The real part of the broad-band impedance in the SPS is only known from threshold measurements of longitudinal turbulence that occurs around 1.3-1.5 *GHz*. A particularity of these measurements is a large spread in the results: from 20 Ω to more than 30 Ω [9,10]. The estimated real part of the impedance *Z/n* (Fig 5) from the ferrite at 1.5 *GHz* is less than 1 Ω, i.e. very small as compared to the measured values. Thus it can be concluded that the ferrite of the kickers does not contribute significantly to the resistive part of the SPS broad-band impedance in the frequency range considered. The main contributors to this impedance are the pumping ports and this should be demonstrated by the ongoing shielding campaign in the SPS.

The imaginary part of the broad-band impedance in the SPS is inductive and amounts to around 20 Ω [9]. As can be seen from Fig. 5, the contribution of the ferrite in the SPS kickers is small and capacitive. It can therefore be concluded that the

kickers are not responsible for the measured imaginary part of the broad-band impedance.

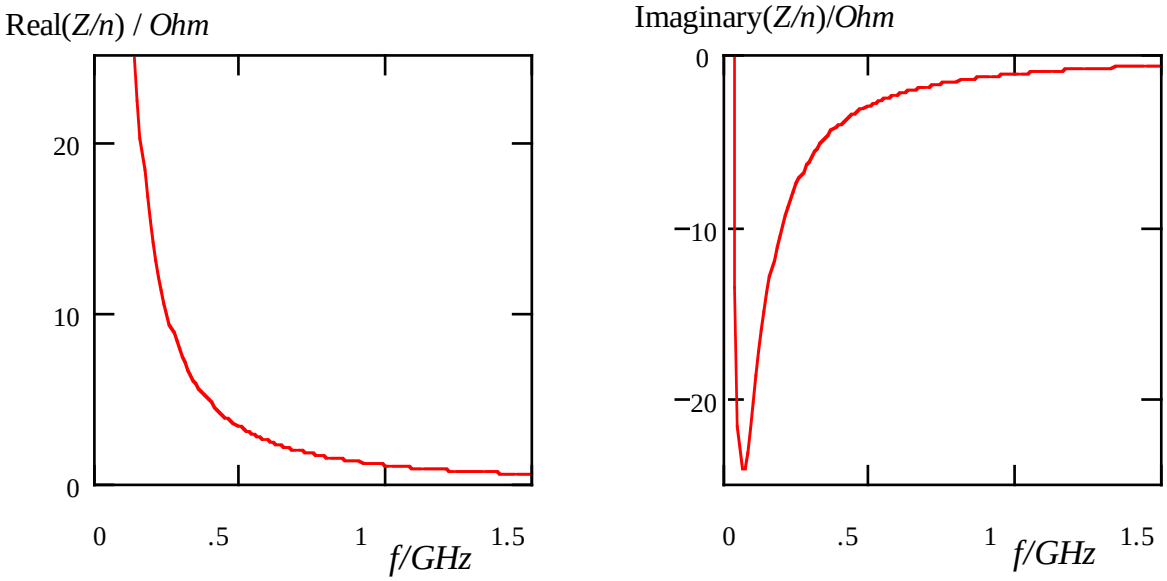

Figure 5 : Real (left) and imaginary (right) part of *Z/n* in SPS from ferrite.

Acknowledgments

I am grateful for the contributions to the final form of this report made by D. Brandt, F. Caspers, F. Ruggiero and H. Tsutsui.

References

[1] R. Feynman, *Cours de Physique*, Electromagnetisme tome 2, Paris InterEditions (1979).
[2] S. Flügge, *Encyclopedia of Physics*, Volume XVIII/2, *Ferromagnetism*, Springer Verlag, Berlin (1966).
[3] J. Smit and H.P.J. Wijn, *Ferrites*, Philips Technical Library, Eindhoven (1959).
[4] L. Landau and E. Lifshitz, Phys. Z. Sowjet. **8**, 337 (1935).
[5] R. Boll, *Wirbelstrom- und Spinrelaxationsverluste in dünnen Metallbändern bei Frequenzen bis zu etwa 1 MHz*, Zeitschr. f. angew. Phys. 10, p 212 (1929).
[6] R. Boll, *Weichmagnetische Werkstoffe*, Vacuumschmelze GMBH, Hanau (1990).
[7] *Soft Ferrites*, Philips Components (1990).
[8] E.C. Jordan and K.G. Balmain, *Electromagnetic Waves and Radiating Systems*, Prentice-Hall, Englewood Cliffs, (1968).
[9] D. Boussard, J. Gareyte, *Measurements of the SPS coupling impedance*, Improvement Report 181 (June 1980).
[10] L. Evans, J. Gareyte, *Limitations of the CERN SPS Collider*, CERN SPS/85-19 (May 1985).
[11] H. Tsutsui, *Some Simplified Models of Ferrite Kicker Magnet for Calculation of Longitudinal Coupling Impedance*, CERN-SL-2000-004 AP, 2000.
[12] T. Bohl, T. Linnecar, E. Chaposhnikova, *Emittance control by modification of the voltage progamme*, SL-MD-Note 246 (1997).
[13] H. P. Westman, *Reference Data for Radio Engineers*, ITT, (1961).
[14] G. Schröder, private communication.

Appendix A Heating of ferrites by proton beams in the SPS

Two temperature measurements (T1 and T2) were performed on a magnet installed in the SPS [14]. The computation of the power deposited in the ferrite based on the model developed in the present report is done in section A1. A calibration measurement is needed to relate dissipated power and temperature rise. The calibration of T1 and T2 are very different and will be discussed in sections A2 and A3. The final summary of the thermal measurements is shown in section 4 where the computed powers are compared with the dissipated powers following from the thermal measurements.

A1 Computation of the power dissipated by a proton beam in a ferrite kicker

The temperature measurements were done on kicker magnets of the MKE type. The geometrical constants of this type of magnet are shown in Table 2. Its resistive impedance can be computed with Eq. 17 and is illustrated in Fig. 6.

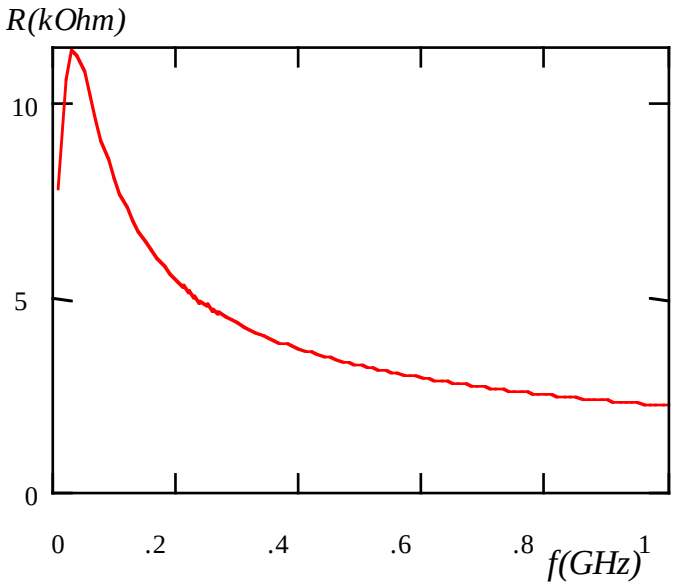

Figure 6 : Resistive impedance of a single MKE kicker magnet

The power dissipation depends on the total intensity of the circulating beam and on the bunch spectrum which is determined by the bunch length. The total beam charge in the two thermal experiments with beam was 1.4 10^{13} (T1) and 1.9 10^{13} (T2) protons respectively, i.e. an average current of I= 0.097 *A* and I= 0.132 *A*. The spectrum for this range of intensities is given in [12] and turns out to be rather constant during the acceleration. This spectrum corresponds to a bunch length of 0.35 *ns*. The active parts of the 14.4 *s* acceleration cycle in the SPS are the ramp (3.3 *s*) and the injection plateau (1.2 *s*). The bunch length during the injection plateau is ~ 0.75 *ns* while the intensity of the beam is at 50 % of the final intensity in the cycle. Hence a duty factor of (0.28+3.3)/14.4=0.245 is assumed with full intensity and a constant bunch length of 0.35 *ns*. Table 3 lists both the relative spectral power of the relevant harmonics of 200 *MHz* and the resistive impedance of the MKE magnet (Eq. 17) including the duty factor (*effective* resistance).

Table 3 : Relative power spectrum for bunches with *rms* length of 0.35 *ns* and *effective* MKE resistance.

frequency	relative power	*effective* resistance
GHz		Ω
0	1	
0.2	0.82	1340
0.4	0.46	898
0.6	0.175	717
0.8	0.045	613
1.0	0.008	544

From the convolution of the spectral power and the effective resistance of the MKE magnet follows the power :

$$P = 3340\, I^2(W). \tag{A-1}$$

The resulting power is 31.4 *W* for T1 and 58 *W* for T2.

2 Thermal calibration measurement for T1[14].

The magnet that was exposed to the beam was equipped with a thermal shield, while the thermal calibration measurements in the laboratory were done on the same unit but without screen. The temperature probes were installed directly on the ferrite. The installation of the thermal screen after the measurements in the laboratory invalidates a straightforward calibration. However, with the help of the considerations that follow it is nevertheless possible to establish suitable calibration factors.

The steady state temperature of a body (kicker) subjected to a constant power flow *P* is given by :

$$T_{ss} = PR_\theta, \tag{A-2}$$

where R_θ is the thermal resistance. The thermal resistance from radiation is given by:

$$R_\theta = \frac{1}{4\varepsilon\sigma_T T_0^3 A}, \tag{A-3}$$

where A is the radiating surface, ε the emissivity of the surface material and σ_T = 5.67 10^{-8} $W/m^2{}^\circ K^4$ is Boltzmann's constant. Assuming an average emissivity ε =0.37, we find for the thermal radiation resistance R_θ = 0.37 $^\circ K/W$.

The thermal time constant is :

$$\tau_\theta = R_\theta C_\theta, \tag{A-4}$$

where C_θ is the thermal capacitance. From the specific heat of ferrite (0.2 $cal/g^\circ C$ = 836 $J/kg/^\circ K$[13]) and the density of the material (5100 kg/m^3 [7]) follows the heat capacitance C_θ =0.19 10^6 $J/^\circ K$ and a time constant τ_θ =19.5 *h*.

From the initial rate of temperature rise under constant power flow the heat capacity of the system can be deduced:

$$C_\theta = \frac{P}{\Delta T^\circ / \Delta t}. \qquad \text{(A-5)}$$

The steady state temperature for a given power yields the thermal resistivity of the system :

$$R_\theta = \frac{\Delta T_{ss}^\circ}{P}. \qquad \text{(A-6)}$$

The magnet in the laboratory was subjected to two different power levels, first at 20 *W*, and then 50 *W*, after a steady state situation at 20 *W* had been achieved. This yields two measurements for C_θ and R_θ, hence of the thermal time constant $\tau_\theta = R_\theta C_\theta$. The results are given in Table 4.

Table 4 : Thermal measurement results on a ferrite kicker body in the laboratory

P	$\Delta T^\circ / \Delta t$	C_θ	ΔT_{ss}	R_θ	τ_θ
W	˚/h	10^6 J/˚	˚	˚/W	h
20	0.36	0.2	6.5	0.32	18
20—>30	0.53	0.2			
50			18.5	0.37	21
computed		0.19		0.37	19.5

The agreement between the computed values and the data from the measurements is rather good.

The magnet was equipped with a thermal shield before installation in the tunnel as was mentioned before. The screen increases the thermal resistance R_θ but it does not change the thermal capacitance C_θ.

A first calibration factor for the magnet in the tunnel is based on the knowledge of the thermal capacitance C_θ. The initial rate of temperature rise during measurement T1 with beam was 0.42 ˚/h. The power according to Eq. A-5, assuming C_θ= 0.2 10^6 J/˚ is then P = 23 *W*.

A second calibration factor is based on the thermal resistance with screen. Its value can be found by dividing the cool-down time by the thermal capacitance. The measured cool-down time was τ_θ = 64 *h* which implies R_θ = 1.15 ˚/W, substantially higher than the thermal resistance without thermal shield as could be expected. From a steady state temperature of ΔT_{ss} = 24.5 ˚ follows a power P = 21 *W* (Eq. A-6).

A3 Thermal calibration measurement for T2[14]

The calibration measurement in the laboratory consisted in heating the core of a MKE kicker magnet with different power levels and observing the increase of the temperature directly on the ferrite (as before) and at the bottom of the alignment tube, accessible from the outside of the vacuum chamber. The results are shown in Table 5.

Table 5 : Steady state temperature increase of ferrite and in alignment tube as a function of power deposition

P	ΔT° in ferrite	ΔT° in alignment tube
W	°	°
30	13.5	5
40	18.2	6.5
50	22.5	8.5
60	26	9.4

The steady state temperature increase in the alignment tube of an identical magnet installed in the tunnel (without thermal shield) that had been exposed to a beam of 0.132 *A* was 9.4°, whereby the variation of the ambient temperature was taken into account. It was concluded that the power deposited in the ferrite by the beam was $P = 60$ *W*.

A4 Summary

Table 6 : Summary of the powers computed with the model of ferrite kicker magnet and of the powers according to two thermal measurements on a MKE magnet exposed to beam in the SPS.

measurement	Average beam current	Power computed with model	Power from thermal measurement
	A	*W*	*W*
T1	0.097	31.4	21
T1	0.097	31.4	23
T2	0.132	58	60

The agreement between the powers computed with the electro-magnetic model and the powers derived from thermal measurements is reasonable. The validity of the model will be further checked by comparing it with new thermal measurements on different types of kickers to be performed as soon as the SPS machine will have restarted.